

A coherent nanomechanical oscillator driven by single-electron tunneling

Yutian Wen,¹ N. Ares,¹ F. Schupp,¹ T. Pei (?),¹ G.A.D. Briggs,¹ and E.A. Laird^{2,1,*}

¹*Department of Materials, University of Oxford, Parks Road, Oxford OX1 3PH, United Kingdom*

²*Department of Physics, Lancaster University, Lancaster, LA1 4YB, United Kingdom*

As electromechanical devices are shrunk towards the nanoscale, the dynamics become sensitive to the force exerted by even individual electrons. Single-electron transistors can transduce mechanical motion with precision approaching the quantum regime. They also introduce feedback leading to backaction noise, dissipation, and electromechanical frequency softening. With sufficiently strong electron-phonon coupling, the feedback instability between these two degrees of freedom leads to [abrupt current jumps and hysteresis?]. Under particular conditions of single-electron tunneling, it is predicted that a DC electrical bias should spontaneously excite a coherent state in a mechanical resonator, synthesising a sustained electrical oscillation on-chip. Here, we demonstrate such an electromechanical oscillator, realised using a quantum dot defined in a vibrating carbon nanotube. The time-resolved observation of the radio-frequency displacement signal from the nanotube exhibits significant coherence, which is limited by telegraph noise and can be further stabilized to second-scale utilizing a passive feedback technique.

As electromechanical devices are shrunk towards the nanoscale (NEMS), the dynamics become sensitive to the force exerted by even individual electrons. Single-electron transistors (SET) can transduce mechanical motion with precision approaching the quantum regime^{1–3}. They also introduce feedback leading to backaction noise, dissipation, nonlinearity and electromechanical frequency softening⁴. With sufficiently strong electron-phonon coupling, the feedback instability between these two degrees of freedom leads to Frank-Condon physics^{5,6} and switching events^{7–11}. Even with weak coupling, it is predicted¹² that a DC electrical bias should spontaneously excite a coherent state in a mechanical resonator via a strong feedback mechanism, synthesising a sustained electrical oscillation on-chip. Here, we present such an electromechanical oscillator, realised using a quantum dot defined in a vibrating carbon nanotube (CNT)¹³. Combining a radio-frequency (RF) readout technique³ with the high sensitivity of a single-electron transistor, we are able to perform time-resolved observation of the resonance, which in turn makes possible the second-long stabilization of the oscillation with a passive feedback mechanism. Our electrically tunable micro-resonator thus holds potential as a platform for future [quantum thermodynamics experiments¹⁴ and as quantum bus for quantum computing^{15,16}].

The experiment setup is schematically shown in Fig. 1a. The resonator is fabricated by stamping a carbon nanotube across lithographically patterned Cr/Au contact electrodes, giving a suspension length of $l = 800$ nm^{3,18–20}. Beneath the nanotube, five predefined Cr/Au finger gates, labelled G1-5 from right to left, allow tuning of the electrical potential along the nanotube. This device is bonded to a printed circuit board and loaded into a 25 mK dilution refrigerator. For electromechanical excitation, gate G2 is connected via a bias tee to an RF drive line and is actuated by an RF signal generator³.

With the source electrode held at ground, a drain-source bias V_{DS} , applied to the drain electrode, drives

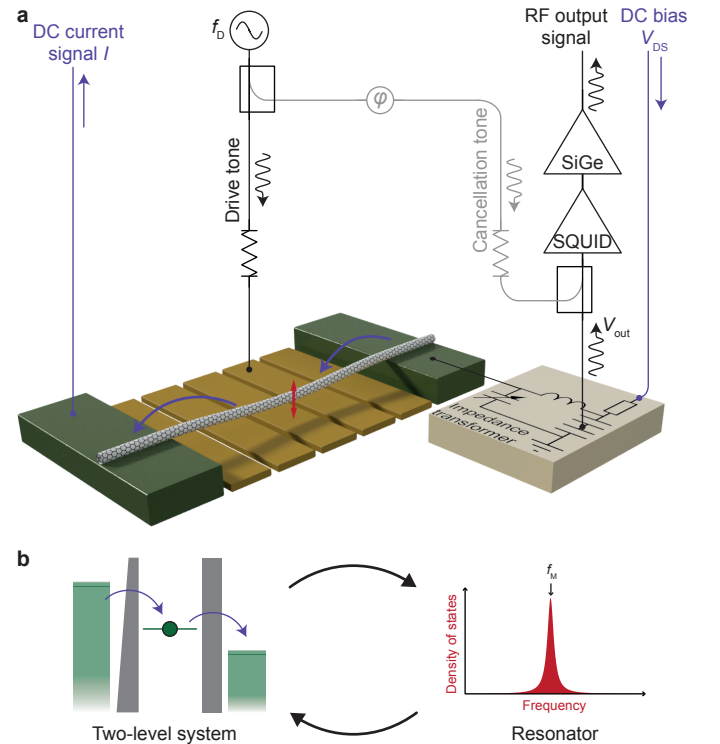


FIG. 1: Schematic diagrams of the experiment overview.

a, Device and measurement setup. Contact electrodes (green) suspend the nanotube, while static DC voltages applied to gate electrodes (yellow) configure the device as a quantum dot in the Coulomb blockade regime. The dot chemical potential is tunable via the DC voltage V_G applied to gate G2. An RF tone is injected to the same gate to actuate the nanotube. To transduce this motion to an electrical current, a bias voltage V_{DS} is applied to the drain contact. The current is monitored both at DC via a room-temperature amplifier (left) and in real-time via an impedance-matching circuit coupled to a radio-frequency measurement setup. The RF output is amplified first by a SQUID amplifier at the base temperature, then a SiGe heterostructure bipolar transistor amplifier anchored at [5 K], before reaching the room temperature³. **b**, Schematic diagram of single-electron tunneling induced mechanical vibration.

a current through the nanotube which can be measured both at DC and at RF. The DC current I is monitored

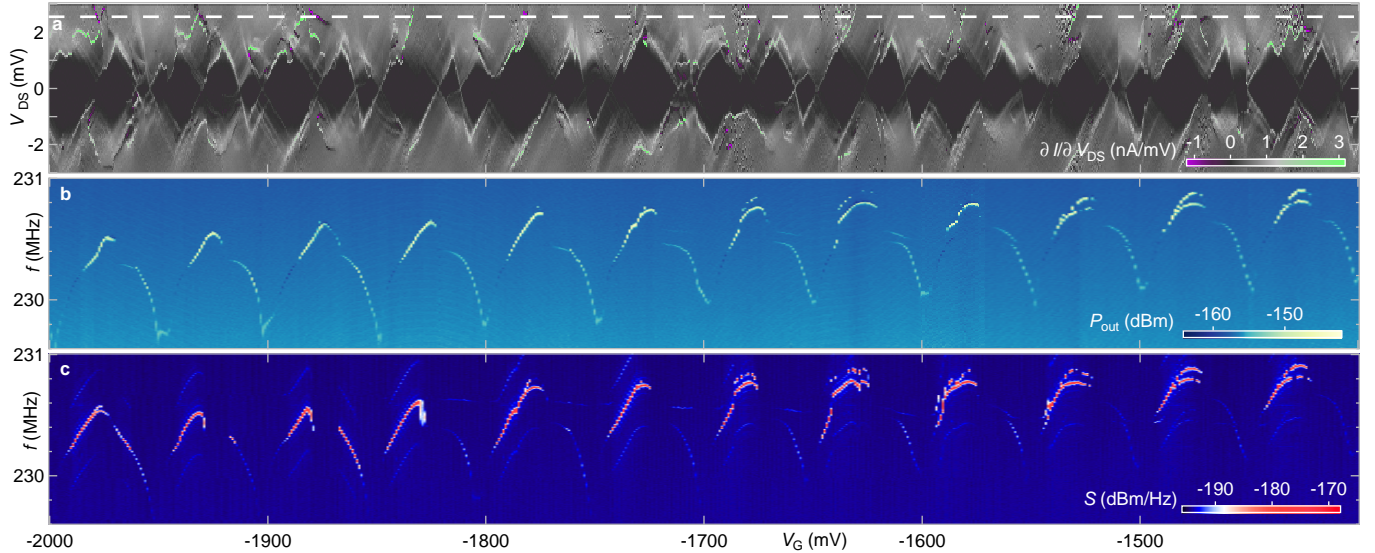


FIG. 2: **a**, The DC Coulomb diamonds. The dashed line marks the bias voltage $V_{DS} = 2.5$ mV where **b,c** are taken. The self-oscillation induced abrupt changes in current, which are highlighted in accent colors. **b**, The transmission spectrum before the SQUID amplifier when the nanotube is driven by $P_{in} = -99$ dBm at the gate. Between the Coulomb softening dips, we see bright self-oscillation signal that aligns with the current ridges in **a**. **c**, The self-oscillation spectrum. No external RF power is applied to the system. The sideband peaks with fixed frequency spacing are due to some mixing effect in the SQUID¹⁷.

using a room-temperature current amplifier connected to the source. The RF part is measured using a SQUID amplifier²¹ at the base temperature, followed by a SiGe heterostructure bipolar transistor (HBT) amplifier²² anchored at [5 K] inside the cryostat. To allow sensitive electromechanical RF measurements, the suspended nanotube is operated as an SET, which is formed between the Schottky barriers along the nanotube and tuned using DC voltages applied to the finger gates^{23,24}. The coordinate displacement of the CNT modulates the electrical potential of the SET, inducing an RF change in the current. To transduce the current change to an RF output voltage V_{out} , a resonant tank circuit (Fig. 1a right)^{3,25}, constructed using chip inductors and capacitors on the circuit board and bonded to the drain electrode, is interposed between the device and the amplifiers. The sensitivity is optimized as the tank circuit's electrical resonance frequency is tuned to near the nanotube mechanical resonance frequency f_M . The tank circuit is characterized in full detail in our technical paper³.

Fig. 1b illustrates the principle of operation of the system as a strong feedback mechanism based on the weak electromechanical coupling between a high Q -factor resonator and the embedded two-level system¹². The mechanical resonator modulates the electrical potential in the SET thus drives the two-level system. In the regime of fast single electron tunneling rate, small oscillation amplitude and low mechanical dissipation [in the cryogenic temperature], the incoherent tunneling dominates the vibration mode linewidth over the geometrical damping and the mechanical nonlinearities^{3,4,13}. The intrinsic energy dependence of the tunnel rate through the semiconductor quantum dot^{26,27} then gives rise to a nega-

tive damping under certain SET voltage conditions. Despite the electromechanical coupling being weak, the high quality-factor of the resonator still enables a strong feedback mechanism, hence the SET in turn populates the vibrational mode, creating an instability. A full theoretical description of the feedback instability was done in Ref.¹², and we give an intuitive deduction in the Supplementary¹⁷.

Figure 2a plots the DC current I through the quantum dot as a function of the DC voltage V_G applied to gate G2. The pattern of current peaks indicates Coulomb blockade, confirming SET behavior. The DC current I jumps abruptly and creates sharp ridges, as highlighted by the accent color. This feature is predicted¹² for where the single-electron tunneling is just strong enough to compensate for the mechanical damping. The oscillation amplitude thus grows resonantly until the amplitude is too large and the SET damping become positive again^{12,17}. When the nanotube switches to a finite oscillation amplitude the average tunneling rate is modified, generating the feature. [We notice accompanying each major Coulomb peak there are some smaller peaks that don't close at zero bias. This is likely due to some defects on the nanotube splitting the charge states spatially, and effectively creating a double quantum dot with a thin middle wall¹⁷].

Turning next to RF measurements. In Fig. 2b we read out the gate-drain transmission, measured using a network analyzer with the tracking power $P_{in} = -99$ dBm at the gate. The electron tunneling overscreens the gate voltage, softening the effective spring constant^{13,28}, so the mechanical signal periodically dips on Coulomb peaks. We notice the sections on the right flank of

each Coulomb peak where the mechanical signal is significantly brighter than that on the left flank, and its frequency increasing further above the mechanical resonance with increasing gate voltage. This part of the signal remains when the nanotube is not externally actuated (Fig. 2c). The fact that the edges of these sections align perfectly with the current ridges in Fig. 2a suggests this might be a single-electron-tunneling-induced coherent oscillation^{12,13}, and indeed we prove the elevated resonance frequency another feature of the self-oscillation behavior in the supplementary¹⁷. A second mode with a slightly higher resonance frequency is visible near $V_G = -1750$ mV, likely due to an orthogonal mode.

The strong gate voltage dependence indicates the signal emanates from the SET. Seeing that the resonator is not externally stimulated by any RF source, it can either be due to thermal excitation or the SET pumping, which would be coherent. To validate the emission coherence, we demodulate the signal using a heterodyne detection circuit (Fig. 3a inset). The signal is mixed with a local oscillator (LO), the frequency of which is offset by $\Delta f = f_M - f_{LO} = 15$ kHz from the mechanical resonance frequency to separate the pink noise from phase slips²⁹. Pass the demodulated signal through low-pass filters (LPFs) that cut-off at 100 kHz, we extract the in-phase (V_I) and quadrature (V_Q) intermediate-frequency (IF) signals. As we fix the bias and sweep V_G across, the nanotube vibrates on and off depending on the gate voltage settings. A pair of example IF traces when the CNT is oscillating is presented in Fig. 3a ($V_G = -1568$ mV). They display clear frequency stability while the signal amplitude and beating interval remain constant. The V_Q trace is visibly delayed by $\pi/2$. We record the IF signal for one second and plot the joint histogram in Fig. 3c. When the nanotube is configured above the threshold, the output RF signal exhibit a ring pattern, characteristic of the coherent emission. The bright spot in the center indicates a bistable state where the CNT stops the oscillation¹², which we will discuss more in the next figure. As a comparison when the negative SET damping does not exceed the threshold, the nanotube does not oscillate (Fig. 4b, $V_G = -1982$ mV), therefore the IF signal shows a thermal distribution centered at zero, proving the signal is not apparatus-originated. This is quantitatively confirmed in Fig. 3d, where we plot the total power histogram for the signal in Fig. 3b,c. The above-threshold emission fits nicely to a gamma waveform while the below-threshold signal fits to a typical exponential decay.

To analyze the phase coherence of the emitted RF signal, we directly calculate the autocorrelation of the IF traces (Fig. 3e). The red trace is fit to a sinusoidal beating with exponentially decaying amplitude $\exp(-t/\tau) \cos(2\pi\Delta ft)$, where the average beating frequency $\Delta f = 13$ kHz and the dephasing time $\tau = 99$ μ s are free parameters. The blue trace is simply an exponential decay, its $\tau = 3$ μ s limited by the lock-in low-pass

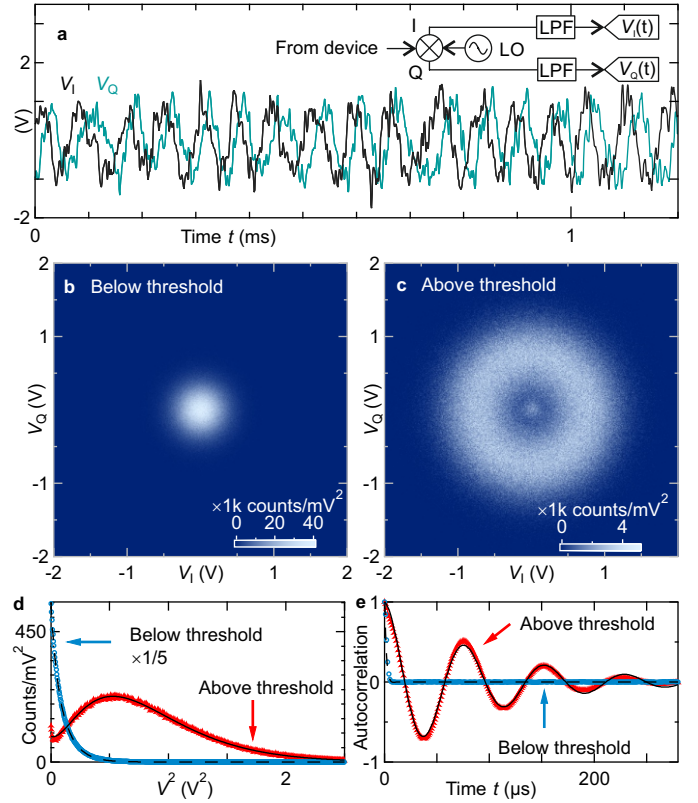


FIG. 3: Coherence properties of the free-running oscillator. **a**, Time traces of the in-phase (I) and the quadrature (Q) component signal from the heterodyne demodulation circuit, as shown in the inset. The amplified emission is mixed with a local oscillator (LO) set to the same nominal frequency, generating two intermediate-frequency (IF) signals corresponding to the in-phase and quadrature components. After filtering and further amplification, these signals are digitised to give the time traces $V_I(t)$ and $V_Q(t)$. The beating frequency $\Delta f = f_M - f_{LO}$ was set to approximately 15 kHz to reduce the $1/f$ noise. **b**, Joint histogram of demodulated components when the gate voltage is set below the oscillation threshold. **c**, Joint histogram for device configured above threshold, showing the ring pattern characteristic of coherent emission. **d**, Points: Histogram of total signal power $V^2(t) = V_I^2(t) + V_Q^2(t)$ above threshold and below threshold (scaled down vertically by a factor of 5). Dashed line: fit to below-threshold data, assuming thermal source. Solid line: Gamma fit to above-threshold data. **e**, Symbols: Autocorrelation function of $V_I(t)$ in **b**, **c**. Solid line: Fit to a sinusoidal beating with exponentially decaying amplitude $\exp(-t/\tau) \cos(2\pi\Delta ft)$, giving coherence time $\tau = 99$ μ s. Dashed line: The exponential decay of coherence when below threshold.

filter.

Now we apply the same analysis to the RF signal across the entire gate voltage range in Fig. 4b. The phase coherence time T_2 is extracted from fitting the second-long IF trace at each point to a slightly different autocorrelation function

$$\alpha \exp(-t/T_2) \cos(2\pi\Delta ft) + (1-\alpha) \exp(-t/\tau_{\text{thermal}}), \quad (1)$$

where the free parameter α scales between 0 and 1 to reflect the proportion of the effective signal in the received power. The second term accounts for the thermal contri-

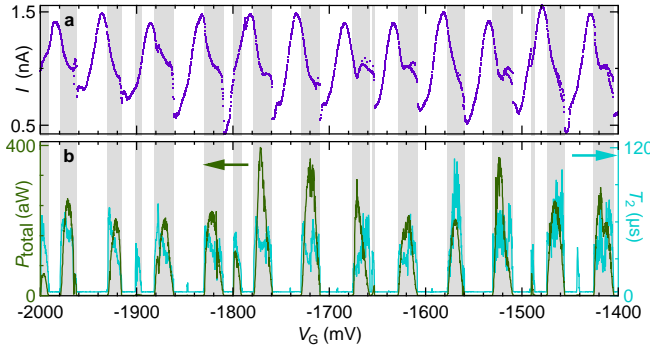


FIG. 4: **Monitoring current through the SET and the self-oscillation emission power and coherence in real time.** **a**, The DC current through the CNT under $V_{DS} = 2.5$ mV. **b**, The corresponding the total self-oscillation power P_{total} (green, left axis) and the coherence time T_2 (cyan, right axis), as a function of the gate voltage.

bution when the nanotube briefly switch off during the data acquisition. The total power P_{total} of the signal is extracted from subtracting a constant noise level off the RF spectrum. We compare these parameters with the tunnel current I in Fig. 4a.

To start with, the signal always exhibits finite coherence time for any finite power, disproving the vibration as thermal-driven Brownian motion. However, above the threshold there doesn't appear to be a general correlation between the emission power and the T_2 in the entire voltage range we investigated. This might be attributed to several other factors that limits T_2 , such as mode coupling and bistability.

We notice the right flanks of the Coulomb peaks in Fig. 4a extends into the partially Coulomb blocked region than the left flank, until it abruptly jumps back to the normal level. Confirming our observation in Fig. 2, the current jump coincide with the voltage region of finite RF power P_{total} (shaded area in Fig. 4b). This phenomenon can be attributed to oscillation-assisted tunneling¹², where more states in the SET open up to tunneling as the vibration displacement significantly modulates the electrical potential.

A final confirmation of the SET-pumped oscillation is the mechanical bistability, which is manifested in both RF and DC current. It is predicted that the resonator energy is bistable in certain configurations, where the nanotube can either stably oscillate with a finitely large amplitude, or with a smaller amplitude which may or may not be zero¹². Theoretically, the switching time from one state to another could be exponentially long¹², but the sweeping gate voltage perturbs the resonator so at each point it randomly settles in either of the allowed states. In DC measurement, the data acquisition is fast (16384 samples / 1 MSa/s) thus the current remains stably in one state. As different vibration amplitude averages to different effective electrical potential, the DC current thus switch between two values in the right part

of Fig. 4a. In fact this is also visible in the same voltage region in Fig. 2a as the Mosaic-like features. In RF measurements, this is explains the double peak pattern in Fig. 2b,c, because the spectrum analyzer is set to a much narrower bandwidth ($RBW = 3/2$ Hz) so the resonator switches between states during the acquisition period, giving rise to the double peak pattern that align with the Mosaic features in DC. It is also responsible for the bright spot in Fig. 3c. Finally in this Figure we notice the RF power P_{total} doesn't vanish when $I/V_G = 0$, a natural consequence of the current being modified by the vibration¹².

In the remainder of this paper we demonstrate two means to lock the emission peak, one involves RF injection while the other is purely passive.

A common way to determine the mechanical resonance frequency of a suspended nanotube is to inject an RF tone to a nearby antenna¹³. By Adler's locking bandwidth equation³⁰, if we sweep the injection frequency f_D , the resonator would be locked to the injection over a range Δf_D which is proportional to the square root of the injection power P_D . When the oscillator is locked, the current through the SET exhibits a sharp peak or dip when f_D matches the mechanical resonance frequency f_M , leading to a feature in the derivative^{31,32} appearing around f_M . When we the DC current exhibit the same sharp features in near the mechanical frequency (Fig. 5a,b). At the same time, the RF resonance peak narrows down to the injection linewidth and locks to the injection frequency over the same frequency range (Fig. 5c,d). Fitting the data at each voltage with $f_D = AP_D^\alpha$, where A and α are free parameters, we find Δf_D doesn't conforms to Adler's prediction, i.e., $\alpha = 1/2$ (dashed line), but instead the scaling exponent α of the nanotube ranges between 0.22 to 0.35 depending on the gate configurations (Fig. 5e). Another unexpected phenomenon is when the resonator is locked, it generates two sideband peaks on either side of the locking tone, marked with white arrows in Fig. 5c,d. Their frequency spacing increases approximately proportional to the [1/4-th] power of the injection power¹⁷.

Alternatively, it is also possible to stabilize the oscillation of the nanomechanical resonator with a passive feedback technique, thank to the sensitive and fast RF readout scheme³ which makes it possible to compare the phase of the emitted signal against the LO in real time. With a sample rate up to 14.06 MHz, the phase difference is then fed into a proportional-integral-derivative (PID) controller³³ which generates a DC control signal between ± 0.8 mV to gate G1 through a LPF that cut-off at 100 kHz.

As displayed in Fig. 6a,b, when this feedback loop is turned on and the PID parameters optimized, the self-oscillation is phase-locked to reference frequency, even though no external RF signal is injected to the system. The linewidth narrows down to less than 2 Hz (Fig. 6b inset), limited by the resolution bandwidth of the spectrum analyzer. In Fig. 6c,d, we sweep the gate voltage

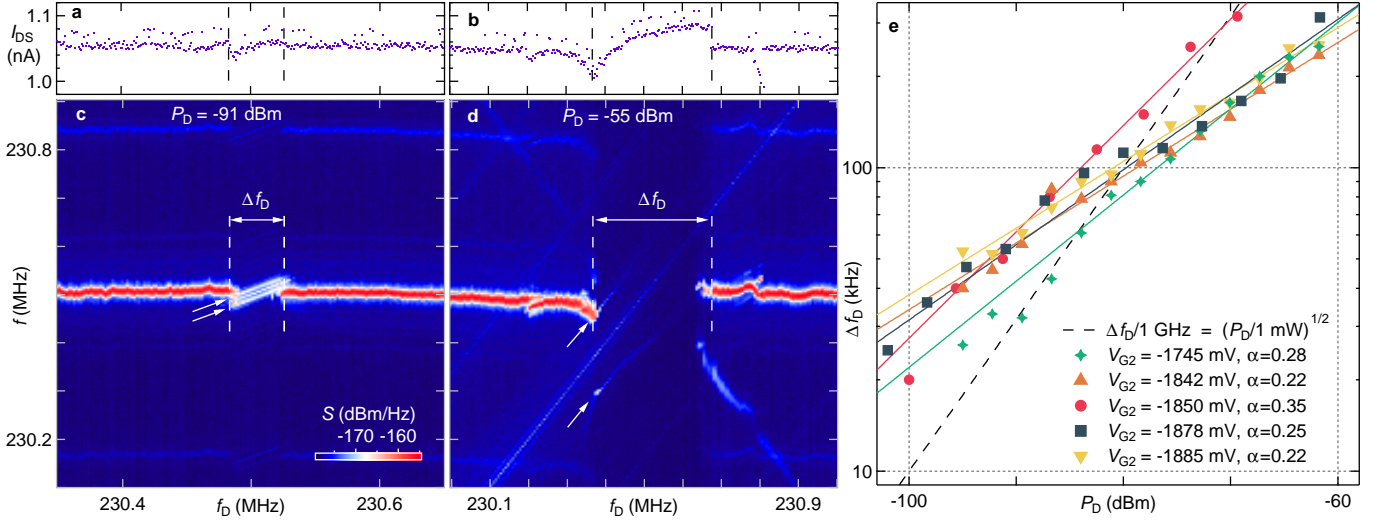


FIG. 5: **RF injection to the gate electrode locks the vibrational frequency.** In **a,c** (**b,d**) we fix the injection power $P_D = -91$ dBm (-55 dBm) and sweep its frequency f_D , the mechanical oscillation will be locked over a certain frequency range Δf_D . The locked state (marked between dashed lines) can be inferred both from the DC current (**a,b**) as well as the RF emission (**c,d**). When the self-oscillation is locked to the injection tone, it also generates two sideband peaks with a varying frequency spacing, as marked with the white arrows. **e**, Symbols: The locking range of the oscillator as a function of the injection power. Solid lines: Fitting the locking range with $f_D = AP_D^\alpha$. The scaling exponent α of the nanotube ranges between 0.22 to 0.35 in various conditions, significantly different from Adler's theory prediction (dashed line).

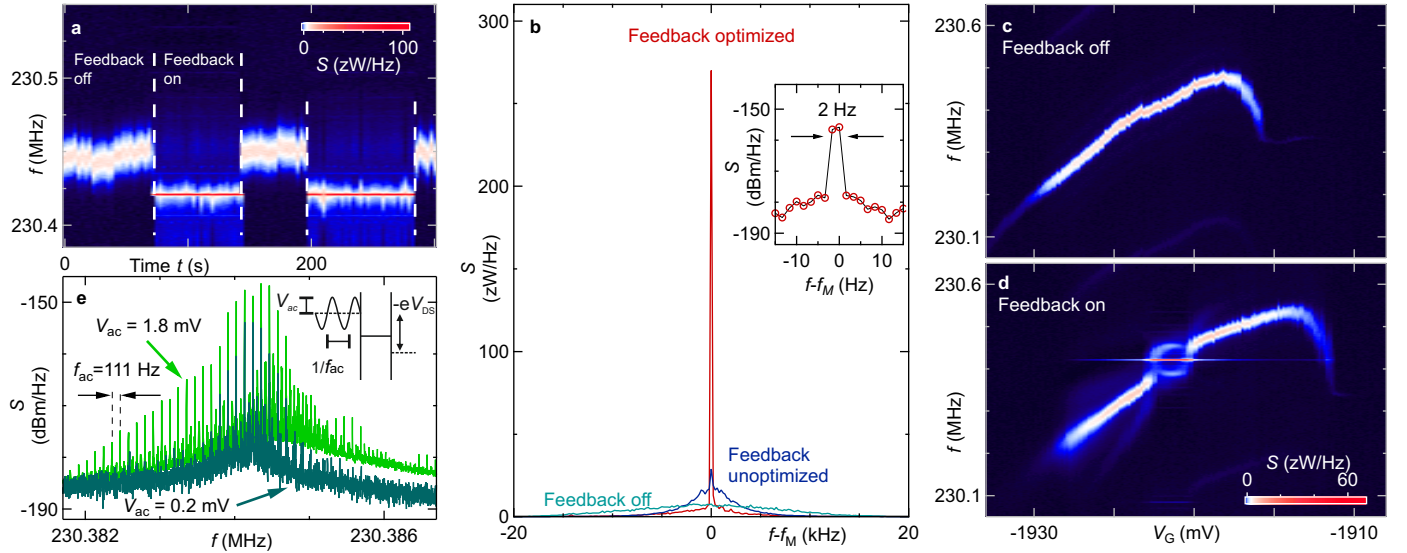


FIG. 6: **Negative-feedback controlled self-oscillation** **a**, The self-oscillation spectrum while the PID feedback loop is turned on and off. The feedback locks the oscillation phase to the local oscillator and narrows the linewidth to one pixel. For the sake of visibility the data is averaged by a 1 kHz window in **a,c,d**. **b**, Self-oscillation spectra when the nanotube is free-running (cyan), partly locked (blue) and optimally locked (red) by the PID loop. When optimally locked the linewidth is less than 2 Hz (inset), limited by the resolution bandwidth. **c,d**, Free running (**c**) and feedback phase-locked (**d**) self-oscillation spectra as functions of the sweeping DC gate voltage. The PID loop is turned on in **d** and the local oscillator is fixed to 230.42 MHz. **e**, By injecting a beating tone $f_{ac} = 111$ Hz to the source we form a frequency comb over a non-linear range of 35 kHz.

over half of a Coulomb peak. When the feedback loop is turned on, the oscillation will be locked to the reference frequency over a certain range, analogous to the situation of RF injection locking ([Fig. S4e]). The sideband peaks again appear. To highlight the locked signal, Fig. 6a,c,d

are averaged by a moving 1 kHz window. As is schematically drawn in the inset of Fig. 6e, we inject an 111 Hz beating signal to the drain, which is mixed with the phase-locked tone and generates a frequency comb over the nonlinearity range.

Unlike the injection locking method, the passive feedback doesn't power the resonator hence the ultra-high quality factor validate the low energy dissipation of the resonator. Since the feedback is DC-filtered, it only cancels telegraph noise that limited the linewidth, such as the surface charge fluctuation. This is in agreement with observation on the frequency stability of a similar device in Ref.³⁴.

Discussion

In the paper we showcased an electromechanical oscilla-

tor using a quantum dot defined in a vibrating carbon nanotube, driven by a strong feedback from the SET despite the electromechanical coupling being weak. The real-time monitoring of the mechanical oscillation made possible a passive resonator stabilization scheme via a DC gate voltage, with which we improved the coherence time to second-scale. This proves the oscillator is not life-time broadened, but instead limited by telegraph noise of the environment.

* Electronic address: e.a.laird@lancaster.ac.uk

- ¹ R. J. Schoelkopf, P. Wahlgren, A. A. Kozhevnikov, P. Delsing, and D. E. Prober, *Science* **280**, 1238 (1998).
- ² M. D. LaHaye, O. Buu, B. Camarota, and K. C. Schwab, *Science* **304**, 74 (2004).
- ³ Y. Wen, N. Ares, T. Pei, G. A. D. Briggs, and E. A. Laird (2018).
- ⁴ H. B. Meerwaldt, G. A. Steele, and H. S. Van Der Zant, in *Fluctuating Nonlinear Oscil. From Nanomechanics to Quantum Supercond. Circuits* (2012), vol. 9780199691, ISBN 9780191742255.
- ⁵ J. Koch, F. Von Oppen, and A. V. Andreev, *Phys. Rev. B* **74** (2006).
- ⁶ E. Burzurí, Y. Yamamoto, M. Warnock, X. Zhong, K. Park, A. Cornia, and H. S. J. Van Der Zant, *Nano Lett.* **14**, 3191 (2014).
- ⁷ F. Pistolesi, Y. M. Blanter, and I. Martin, *Phys. Rev. B* **78** (2008).
- ⁸ A. Mitra, I. Aleiner, and A. J. Millis, *Phys. Rev. B* **69** (2004).
- ⁹ D. Mozyrsky, I. Martin, and M. B. Hastings, *Phys. Rev. Lett.* **92**, 4 (2004).
- ¹⁰ D. Mozyrsky, M. B. Hastings, and I. Martin, *Phys. Rev. B* **73** (2006).
- ¹¹ C. Doiron, W. Belzig, and C. Bruder, *Phys. Rev. B* **74**, 205336 (2006).
- ¹² O. Usmani, Y. M. Blanter, and Y. V. Nazarov, *Phys. Rev. B* **75** (2007).
- ¹³ G. A. Steele, A. K. Hüttel, B. Witkamp, M. Poot, H. B. Meerwaldt, L. P. Kouwenhoven, and H. S. J. van der Zant, *Science* **325**, 1103 (2009).
- ¹⁴ R. Alicki and R. Kosloff (2018).
- ¹⁵ J. Majer, J. M. Chow, J. M. Gambetta, J. Koch, B. R. Johnson, J. A. Schreier, L. Frunzio, D. I. Schuster, A. A. Houck, A. Wallraff, et al., *Nature* **449**, 443 (2007).
- ¹⁶ A. D. O'Connell, M. Hofheinz, M. Ansmann, R. C. Bialczak, M. Lenander, E. Lucero, M. Neeley, D. Sank, H. Wang, M. Weides, et al., *Nature* **464**, 697 (2010).
- ¹⁷ See supplementary material.
- ¹⁸ C. C. Wu, C. H. Liu, and Z. Zhong, *Nano Lett.* **10**, 1032 (2010).
- ¹⁹ F. Pei, E. A. Laird, G. A. Steele, and L. P. Kouwenhoven, *Nat. Nanotechnol.* **7**, 630 (2012).
- ²⁰ A. Mavalankar, T. Pei, E. M. Gauger, J. H. Warner, G. A. Briggs, and E. A. Laird, *Phys. Rev. B* **93**, 235428 (2016).
- ²¹ F. J. Schupp, N. Ares, A. Mavalankar, J. Griffiths, and

- G. A. C. Jones, **1**, 1 (2018).
- ²² N. Ares, T. Pei, A. Mavalankar, M. Mergenthaler, J. H. Warner, G. A. Briggs, and E. A. Laird, *Phys. Rev. Lett.* **117**, 170801 (2016).
- ²³ N. Mason, M. J. Biercuk, and C. M. Marcus, *Science* **303**, 655 (2004).
- ²⁴ E. A. Laird, F. Kuemmeth, G. A. Steele, K. Grove-Rasmussen, J. Nygård, K. Flensberg, and L. P. Kouwenhoven, *Rev. Mod. Phys.* **87**, 703 (2015).
- ²⁵ N. Ares, F. J. Schupp, A. Mavalankar, G. Rogers, J. Griffiths, G. A. Jones, I. Farrer, D. A. Ritchie, C. G. Smith, A. Cottet, et al., *Phys. Rev. Appl.* **5**, 034011 (2016).
- ²⁶ K. MacLean, S. Amasha, I. P. Radu, D. M. Zumbühl, M. A. Kastner, M. P. Hanson, and A. C. Gossard, *Phys. Rev. Lett.* **98** (2007).
- ²⁷ M. R. Astley, M. Kataoka, C. J. Ford, C. H. Barnes, D. Anderson, G. A. Jones, I. Farrer, D. A. Ritchie, and M. Pepper, *Phys. Rev. Lett.* **99** (2007).
- ²⁸ B. Lassagne, Y. Tarakanov, J. Kinaret, G. S. Daniel, and A. Bachtold, *Science* **325**, 1107 (2009).
- ²⁹ M. C. Cassidy, A. Bruno, S. Rubbert, M. Irfan, J. Kammhuber, R. N. Schouten, A. R. Akhmerov, and L. P. Kouwenhoven, *Science* **355**, 939 (2017).
- ³⁰ R. Adler, *Proc. IRE* **34**, 351 (1946).
- ³¹ V. Sazonova, Y. Yaish, H. Üstünel, D. Roundy, T. A. Arias, and P. L. McEuen, *Nature* **431**, 284 (2004).
- ³² A. K. Hüttel, G. A. Steele, B. Witkamp, M. Poot, L. P. Kouwenhoven, and H. S. J. Van Der Zant, *Nano Lett.* **9**, 2547 (2009).
- ³³ K. Ogata and Y. Yang, *Modern control engineering*, vol. 4 (Prentice hall, 1970).
- ³⁴ J. Schwender, I. Tsioutsios, A. Tavernarakis, Q. Dong, Y. Jin, U. Staufer, and A. Bachtold, *Appl. Phys. Lett.* **113** (2018).

Acknowledgements We acknowledge E. M. Gauger for discussions and T. Orton for technical support. This work was supported by EPSRC (EP/N014995/1, EP/R029229/1), DSTL, Templeton World Charity Foundation, and the Royal Academy of Engineering.

Author Contributions